PCCP

Accepted Manuscript

ROYAL SOCIETY OF CHEMISTRY

www.rsc.org/pccp

Unravelling the Correlated Electronic and Optical Properties of $BaTaO_2N$ with Perovskite-Type Structure as a Potential Candidate for Solar Energy Conversion

Ahmed M. Hafez, Noha M. Salem and Nageh K. Allam*

Energy Materials Laboratory, Physics Department, School of Sciences and Engineering, The American University in Cairo, New Cairo 11835, Egypt

Abstract

We report on the first principles calculation of the electronic, structural and optical properties of $BaTaO_2N$, using density functional theory (DFT) and Finite Difference Time Domain (FDTD) methods. Band structure calculations were performed to calculate the direct and indirect bandgaps of the material. Density of states and Mulliken charge analysis as well as the electronic contour maps were established to determine the type of bonding and hybridization between the various electronic states. The dielectric constant, reflectivity, absorption, optical conductivity and energy-loss function were also calculated. Moreover, FDTD was used to investigate the optical properties of a larger and more reliable structure for $BaTaO_2N$ powder with a good agreement with the reported experimental parameters. The calculated electronic, structural and optical properties showed the potential of $BaTaO_2N$ for solar energy conversion and optoelectronic applications.

Keywords: $BaTaO_2N$; perovskite; optical; electronic; DFT; FDTD; solar.

*Author to whom correspondence should be addressed. Electronic mail: nageh.allam@aucegypt.edu

Introduction

Perovskites have the general formula ABO_3, where the A atoms are placed at the corners of the cubic crystal lattice, the B atoms are placed at the center, and the oxygen atoms are positioned at the center of the faces [1]. Perovskites have very interesting properties including their superconductivity, high dielectric properties, and excellent electronic transport features [2,3]. However, most of the perovskites are wide bandgap materials due to the fundamental characteristics of the metal–oxygen (A–O and B–O) bonds. The excitation across the bandgap is essentially a charge transfer from the oxygen O 2p states at the valence band maximum to the transition-metal d states at the conduction band minimum. Owing to the large difference in electronegativity between the oxygen and transition-metal atoms, the bandgap is quite large (3–5 eV) [4]. This wide bandgap limits their use as photoactive materials, especially in solar energy conversion devices.

Following the bandgap-engineering strategy explored in semiconductor materials [5,6]. doping perovskites with nitrogen to form the corresponding oxynitrides seems to be of potential interest. Oxynitrides are expected to have lower bandgap compared to the oxide counterparts owing to the higher N 2p orbital energy than that of the O 2p orbitals. Moreover, the comparable size and charge between O and N give unusual bonding preference [7], resulting in better performance of the oxynitrides over the pure metal-oxide or pure-nitride counterparts, making perovskite oxynitrides suitable candidates for solar energy conversion [8].

Barium tantalum oxynitride ($BaTaO_2N$) has a perovskite-like structure[9-12], with band gap energy of 1.8 eV, making it a suitable choice as an active material in solar energy conversion devices. For solar water splitting, Higashi *et al.* [13] , were able to achieve an IPCE value of 10% (at 1.2 V_{RHE}) using $BaTaO_2N$ photoanodes co-loaded with CoO_x and RhO_x nanoparticles, which is among the highest photoanode materials with band gap smaller than 2 eV. On the other hand, $BaTaO_2N$ has a high and temperature-independent dielectric constant

both in polycrystalline and thin film forms, giving it a dielectric property that is suitable for designing miniaturized and elegant devices [14] related the unusual dielectric properties of cubic perovskite $BaTaO_2N$ to the local polarizations induced by the geometry relaxations, which stem from the local atomic displacements[15,16]

Once the relationship between atomic compositions, structural and material properties is well defined, new materials which improve upon the existing technology can be designed. To this end, quantum mechanical simulations and accurate molecular dynamics models are essential to understand in more details the electronic, structural and optical properties of $BaTaO_2N$. Herein, we coupled the density functional theory (DFT) calculations with the finite difference time domain (FDTD) simulations to unravel the correlated electronic and optical properties of perovskite $BaTaO_2N$. To the best of our knowledge, this is the first investigation on the use of first principles calculation to study the optical properties of $BaTaO_2N$.

Computational Details

The calculations were performed in the framework of the density functional theory (DFT) as implemented in CASTEP code[17]. The calculations were carried out for the structure including the crystal periodicity in the DFT code. Normconserving pseudopotential with plane wave basis sets has been used with the exchange correlation energy term approximated using generalized gradient approximation (GGA) according to Perdew-Burke-Ernzerhof [18,19], which includes the gradient in the charge density throughout the crystal. The structure is geometry optimized with cut-off energy of 750 eV, and $3 \times 3 \times 3$ k-point grid is used. The energy tolerance between successive iterations was $1 \text{ X } 10^{-6}$ eV/atom, the maximum force between atoms was set to 0.003 eV/Å, where the maximum displacement tolerance was 1×10^{-3} Å, and the maximum stress was 0.05 GPa. The band structure and density of states are

calculated using the same functional. Population analysis is performed using the Mulliken formalism [20]. The FDTD is used to investigate the material from a larger scale point of view. The source used for the simulation was Gaussian source with central frequency of 753.45 THz. The dielectric function obtained from the DFT calculations is approximated to drude-lorentizian model to be used for the time domain modeling. The $BaTaO_2N$ powder is modeled by a set of identical spheres with diameter of 200 nm each, deposited over ITO substrate. The dielectric function for ITO is obtained from the experimental results [21]. The geometry cell used in the simulation is surrounded with a perfect matched layer (PML) that acts as a perfect absorber against the wave scattering. The structure is designed to model the real case, where the light is incident on the ITO substrate then propagate through the $BaTaO_2N$ powder.

Results and Discussion

$BaTaO_2N$ is one of the compounds that belong to the $BaTiO_3$ perovskite group structures [22], where one O^{2-} ion is replaced by one N^{3-} ion, such that the anionic charge is balanced by exchanging Ti^{4+} against Ta^{5+}. $BaTaO_2N$ has cubic perovskite structure with ($pm\bar{3}m$) space group [15], as shown in Figure 1a. The $BaTaO_2N$ optimized structure is obtained by full relaxation of the unit cell with its lattice parameters. Table I compares the parameters of the optimized structure with those reported experimentally [11]. Ta is bonded to four oxygen atoms and two nitrogen atoms in a N-Ta-N straight line (180°) [11, 23]. This structure gives the most approximate optical properties compared to those reported experimentally. Note that Fang *et al*[23] reported small differences in the electronic structures of the ordered and randomly distributed O/N structures of $BaTaO_2N$.

The use of plane wave basis sets gives a delocalized nature for the energy state without any information about the localization of electrons inside the crystal, lacking the

ability to estimate the electronic properties such as bond population, atomic charge etc. However, a technique illustrated by Sanchez *et al.* [24] showed the projection of the delocalized basis sets onto a localized basis, by which a reliable population analysis can be made using the resulted projected states as that performed using Mulliken formalism [20]. This method is widely used for investigating the electronic structure and the atomic orbitals based on the linear combination of atomic orbitals method. The results of the obtained Mulliken charge and population is listed in Table II. The charge localized around the O1, O2 and N atoms are -0.77, -0.76, and -0.88, respectively. Therefore, the N atom has the largest electron affinity inside the structure, while Ta has the most positive value (1.26). This is in agreement with the population analysis, which shows a covalent bond behavior along the N-Ta bond (0.72) as well as O1-Ta (0.47) and O2-Ta (0.48) bonds. Moreover, there is a week bonding between O1-Ba, O2-Ba and N-Ba atoms (0.08, 0.09 and 0.18, respectively). In addition, the N-O bond shows negative overlapping populations (-0.14), which indicates the presence of anti-bonding molecular orbitals between these two atoms. These results are further confirmed by calculating the bond length along the pairs of atoms. The O1-Ta bond length is 2.32061Å indicating its covalent bonding behavior, while the N-Ba bond length is 2.73465 Å indicating a week bonding between N and B atoms. However, in the anti-bonding case, N-O bond length has the largest value of 2.85941 Å.

Figure 1b shows the obtained band structure of $BaTaO_2N$, which shows an indirect band gap of 1.53 eV, where the conduction band minimum (CBM) is located at the highest symmetry point gamma (G), and the valence band maximum (VBM) is located along the symmetry line Z→G near the gamma point. The direct band gap is 1.6 eV, which is very close to the reported experimental bandgap of 1.8 eV [15]. Note that our calculation method for $BaTaO_2N$ $pm\bar{3}m$ structure reduces the error in the bandgap estimation from 72 % [23], and 61%

[25] to only 15%. This is expected to help more investigations into the electronic and structural properties of the material, especially if modified with foreign atoms.

Figure 1c shows the obtained total and partial density of states of $BaTaO_2N$. It shows a wide valence band (about – 20 eV) that is consisted of three sub bands. A low band (-19 eV to -17 eV) mainly formed by the O 2s states, which is weakly dsp-hybridized with Ta 6s, 6p and 5d states. A middle sub-band (-14 eV to -9 eV) formed by the hybridization of N 2s states with Ba 5p states with small contribution from the Ta 5d states. A maximum valence sub-band (-6 eV to 0 eV) formed by the hybridization of Ta 5d , N 2p and O 2p states. This hybridization shows strong covalence between Ta and O as well as N atoms, which is in agreement with the Mulliken charge analysis. It can be observed that the VBM strongly depends on the energy of the N 2p states, which has the main role in determining the position of the VBM in $BaTaO_2N$. The conduction band extends from 2 eV to 14 eV, where the CBM is dominated by Ta 5d states. However, the hybridization takes place between Ta 5d, Ba 4d, N 2p and O 2p states from 3 eV to 11 eV, with small contributions from Ba 6s, Ta 6s, and Ta 6p states. The highest unoccupied conduction band states are formed by Ta 6p and Ta 6s orbitals. From the partial density of states (PDOS), the bonding and anti-bonding states around the VBM and CBM energy levels show a symmetric distribution for Ta 5d, N 2p and O 2p states, which is related to the difference in the energies between these states, as indicated from the Mulliken analysis. We find also that Ba has no effect on the band gap positioning in $BaTaO_2N$, and its effect appears only at the deep anti-bonding states.

For further investigating the bonding and anti-bonding states, the projected contour maps for the electronic wave function on different three planes were obtained as shown in Figure 2. Note that the three pairs of slices are presented to show all the possible combinations between Ta, O, N, and Ba atoms. Figure 2a shows the charge density distribution for a slice containing Ta, O, and N. This slice shows the strong covalence between Ta-O and Ta-N pair of atoms,

which was previously verified from the electron affinity in the population analysis as well as the hybridization in the calculated PDOS at VBM between Ta 5d, N 2p, and N 2p states. We believe that this strong covalent bond plays the main role in determining the position of the VBM in $BaTaO_2N$. Figure 2b shows the anti-bonding states at the same slice at the conduction band. Note that there is no bonding between these three atoms, where each atomic charge is uniformly distributed around its atom. Figure 2c shows the slice that reveal Ta, O and Ba, where covalence bonding between the Ta and O atoms through the hybridization between Ta 5d and O 2p states is clear. However, there is no interaction between both atoms and Ba. Figure 2e shows the slice that includes N and Ba atoms, where there is a very week bonding between N and Ba through the hybridization of N 2s and the deep Ba 5p states. Figure 2d,f shows the anti-bonding states in (Ta, O, Ba) and (N, Ba) slices, respectively, indicating also the anti-bonding properties in these hybridized states.

Owing to its bandgap, $BaTaO_2N$ is considered as a potential material for optical and optoelectronic applications. Therefore, it is crucial to investigate its optical properties in more details. In this regard, the complex dielectric function ε(ω) can be described as: [26]

$$\varepsilon = \varepsilon_1 + i\varepsilon_2 = N^2 \qquad (1)$$

where ε_1 and ε_2 are the real and imaginary parts of the dielectric constant, respectively. The calculation of the imaginary part of the dielectric function is estimated using the following relation: [26,27]

$$\varepsilon_2(\omega) = \frac{2e^2\pi}{\Omega\varepsilon_o} \sum_{\kappa,v,c} \left|\langle \psi_\kappa^c \left| H' \right| \psi_\kappa^v \rangle\right|^2 \delta\left(E_\kappa^c(\vec{k}) - E_\kappa^v(\vec{k}) - \hbar\omega\right) \qquad (2)$$

where Ω is the unit cell volume, $\hbar\omega$ is the photon energy, H' is the matrix element for the electromagnetic perturbation added to the normal Hamiltonian taken between the valence and

conduction band Bloch states at wave vector $\vec{k}$, and the δ-function is the energy conservation at $\vec{k}$.

In particular, the imaginary part is calculated first, from which the real part $\varepsilon_1(\omega)$ can be obtained by the Kramers-Kronig transform, using the fact that the dielectric constant describes a causal response. The dielectric constant $\varepsilon(\omega)$ is a function of the frequency (ω), classifying ε into electronic contribution part ($\varepsilon_{\omega\to\infty}$), and lattice vibrational contribution part ($\varepsilon_{\omega=0}$), or the optical and static molecular polarizability. Figure 3 shows the calculated real and imaginary parts of the diagonal components of the dielectric tensor; ε^{xx} , ε^{yy} and ε^{zz} . Note that ε^{xx} and ε^{yy} are isotropic with the same value, whereas ε^{zz} reveal anisotropic behavior in the range 0-20 eV. The first optical components appear at 3.758 eV for ε^{zz} and 7 eV for ε^{xx} and ε^{yy}. The electronic contribution for ε^{zz} is 9.647, which is much greater than that of the other two diagonal components (5.543). Therefore, ε^{zz} plays the major role in the electronic transition from VBM to CBM states [28]. These results show that $BaTaO_2N$ has large dielectric constants in the [001] direction, which add promising dielectric property to the material, allowing its use as a highly dielectric material in many photonic applications. We observed also that the diagonal ε^{zz} component has a negative peak around 5 eV, where the structure gains a metallic property, making it capable to attract similar charges with unusual scattering to the incident electromagnetic waves in that direction [001] around this range of frequencies.

Based on the calculated dielectric constants, the other optical properties can then be obtained using the following relations: [29]

$$R(\omega) = \left|\frac{\sqrt{\varepsilon_1(\omega)+j\varepsilon_2(\omega)}-1}{\sqrt{\varepsilon_1(\omega)+j\varepsilon_2(\omega)}+1}\right|^2 \quad (3)$$

$$\alpha(\omega) = \sqrt{2}\omega\left[\sqrt{\varepsilon_1^2(\omega) + \varepsilon_2^2(\omega)} - \varepsilon_1(\omega)\right]^{\frac{1}{2}} \quad (4)$$

$$n(\omega) = \left[\sqrt{\varepsilon_1^2(\omega) + \varepsilon_2^2(\omega)} + \varepsilon_1(\omega)\right]^{\frac{1}{2}}/\sqrt{2} \quad (5)$$

$$k(\omega) = \left[\sqrt{\varepsilon_1^2(\omega) + \varepsilon_2^2(\omega)} - \varepsilon_1(\omega)\right]^{\frac{1}{2}}/\sqrt{2} \quad (6)$$

$$L(\omega) = \varepsilon_2(\omega)/[\varepsilon_1^2(\omega) + \varepsilon_1^2(\omega)] \quad (7)$$

Figure 4a-e shows the calculated refractive index $n(\omega)$, extinction coefficient $k(\omega)$, absorption coefficient $\alpha(\omega)$, reflectivity $R(\omega)$ and the energy-loss spectrum $L(\omega)$, respectively. The reflectivity spectrum (Figure 4a) shows three sharp peaks at 5, 11 and 13 eV. Another two closed peaks located at 23 and 25 eV, with higher intensities than those observed at low energy. The low frequency peaks arise mainly from the inter-band transitions of the hybridization between Ta 5d, N 2p and O 2p states. However, the higher frequency peaks arise from the transition between the VBM and the CBM states. The reflectivity vanishes at frequencies greater than 40 eV. The index of refraction, which determines the light bending or refracted from the $BaTaO_2N$ (Figure 4b), shows two distinct peaks at 5 and 9 eV, with a static value of 3.5 at n(0). The extinction coefficient $k(\omega)$ (Figure 4c) indicates the amount of absorption loss when the electromagnetic wave propagates through $BaTaO_2N$, which shows three peaks at 2.5, 10.5 and 19 eV. Moreover, with low photon energy (0-1.6 eV), $k(\omega)$ has a value of zero, consistent with the size of the band gap. The absorption coefficient (Figure 4d) also reveals a large increase above the band gap value as an indication for electron-hole pair threshold energy, and the transition of electrons from the valence to conduction band. The optical conductivity with its real and imaginary parts is also shown in Figure 4e. The real part represents the in-phase current, that produces the resistive heating energy, while the imaginary part represents the (π/2) out-of-phase inductive current. The

examination of $Re(\sigma)$ and $Im(\sigma)$ as functions of the frequency shows that in the frequency region 0-19 eV , $Im(\sigma)$ is less than $Re(\sigma)$.That is, The electrons in this range reveal a resistive character. However, in the frequency region 20-40 eV, $Im(\sigma)$ is larger than $Re(\sigma)$, at which, the electrons reveal an inductive character. At this range there is no energy absorbed from the field, and no joule heat appears. The real part $Re(\sigma)$ also has three successive peaks at 5, 11 and 20 eV, respectively. The electron energy-loss function, representing the loss of energy of a fast moving electron inside the material, is shown in (Figure 4f). It has an obvious peak at 25 eV, which is known as the plasma frequency above which the material is considered a dielectric $[\varepsilon_1(\omega) > 0]$, and below which the material behaves as a metallic material $[\varepsilon_1(\omega) > 0]$.

The optical properties discussed so far are related to the molecular scale for $BaTaO_2N$. However, a difference usually exists between the molecular scale and the macro-scale structures. In fact, the density functional theory cannot be easily used for the simulations of such large structures, because of the huge computational cost required. Therefore, it is more convenient to investigate the optical properties for this structure using another technique such as Finite Difference Time Domain (FDTD) [30]. FDTD is a computational method that is used to model the optical properties of materials with various dimensions and shapes, through a wide spectral range. This method, based on time-dependent Maxwell's equations, is one of the differential numerical time domain modeling methods, where the electric field is initially solved, by which the magnetic field is obtained, then the values of the electric and magnetic field is updated with the propagating time domain, through a mesh lattice grid, well-known as Yee's lattice [31]. Since FDTD periodically solve the electrical and magnetic field with time throughout the simulation domain, it can be also used to provide an animated display for the electromagnetic propagation inside the material.

This is of great interest that helps in understanding in more details how the material behaves with the incident electromagnetic wave.

Figure 5a shows a schematic diagram for the simulated $BaTaO_2N$ powder. $BaTaO_2N$ powder is represented by spheres with diameters of 200 nm, with a total deposited layer thickness of 800 nm. This layer is assumed to be deposited on indium-doped tin oxide (ITO) substrate with a thickness of 400 nm. The transmission and reflection planes are placed to measure the transmitted and reflected electromagnetic waves out of the source through the material. The dielectric function for $BaTaO_2N$ used in the simulations is that obtained from the DFT calculations. This function is approximated to the Drude-lorentezian model in order to be used in the time domain modeling. The simulated transmittance, reflectance and absorbance are shown in Figure 5b. The absorbance curve shows the good absorbing properties of the material in the visible light region, near 600 nm. This result demonstrates the capability for $BaTaO_2N$ to harvest a large percentage of the visible light, and strengthen its use as a photoactive layer over other comparatives[15]. The reflectance is also significantly high, probably because of the dielectric mismatch between the ITO substrate, $BaTaO_2N$ powder and air. The transmittance is starting from 375 nm above which the absorbance inside the material is gradually decreased, resulting in a large transmitted field value. Figure 5b reveals the propagation of the electromagnetic wave through $BaTaO_2N$ at different time instants. The figure shows the variation in the EM wave strength throughout the simulation interval. The $BaTaO_2N$ powder is represented as small spheres inside the propagated field, at which the wave shows significant damping in its strength, as a result of the absorption at the wavelengths mentioned above. This should give a detailed prediction about the behavior of this material with the incident solar spectrum, Figure 5c.

Summary and Conclusions

In this study, first principle calculations were used to investigate the structural and optical properties of $BaTaO_2N$. Our lattice parameters and atomic positions for the optimized structure show a good agreement with the reported experimental values. The calculated direct and indirect band gaps were 1.53 and 1.6 eV, respectively. Mulliken charge analysis is established to show the bond types and arrangements between the different atoms. The bond types are further illustrated through the contour maps for the electronic wave functions. The partial and total density of states described in more details how the bonding and the anti-bonding states are formed and the hybridizations between the valence and conduction energy of states is also shown. The VBM was found to strongly depend on the energy of the N 2p states. The hybridization takes place between Ta 5d, Ba 4d, N 2p and O 2p states from 3 eV to 11 eV, with small contributions from Ba 6s, Ta 6s, and Ta 6p states. Ba was found to have no effect on the band gap positioning in $BaTaO_2N$, and its effect appears only at the deep anti-bonding states. Moreover, the results show that $BaTaO_2N$ has large dielectric constants in the [001] direction. Finally, we investigated how the $BaTaO_2N$ powder behaves with the incident electromagnetic waves through the modeling of this macro-scale structure using FDTD, giving the overall transmittance, reflectance and absorbance. Our investigation gives detailed information about $BaTaO_2N$ structural and optical properties, showing its promising capability to be used as a photoactive material in solar energy conversion and optoelectronic devices.

Acknowledgment

This work was made possible by NPRP grant # NPRP 6 - 351 - 1 - 072 from the Qatar National Research Fund (a member of Qatar Foundation).

References

[1] Pena, M. A.; Fierro, J. L. G. Chemical Structures and Performance of Perovskite Oxides. *Chem. Rev*. **2001**, *101*, 1981-2018.

[2] Maeno, Y.; Hashimoto, H.; Yoshida, K.; Fujita, T; Bednorz, J. G.; Lichtenberg, F. Superconductivity in A layered Perovskite Without Copper. *Nature* **1994**, *372*, 532-534.

[3] Kozuka, H.; Yamada, H.; Hishida, T.; Yamagiwa, K.; Ohbayashi, K.; Koumoto, K. Electronic Transport Properties of the Perovskite-Type Oxides $La_{1-x}Sr_xCoO_{3\pm\delta}$. *J. Mater. Chem.* **2012**, *22*, 20217-20222.

[4] Grinberg, I.; Vincent, D.; Torres, M.; Gou, G.; Stein, D. M.; Wu, L.; Chen, G.; Gallo, E. M.; Akbashev, A. R.; Davies, P. K.; Spanier, J. E.; Rappe, A. M. Perovskite Oxides for Visible-Light-Absorbing Ferroelectric and Photovoltaic Materials. *Nature* **2013**, *503*, 509-512.

[5] Allam, N. K.; Shaheen B. S.; Hafez, A. M. Layered Tantalum Oxynitride Nanorod Array Carpets for Efficient Photoelectrochemical Conversion of Solar Energy: Experimental and DFT Insights. *ACS Appl. Mater. Interfaces* **2014**, *6*, 4609-4615.

[6] Huda, M.; Yan; Yanfa; Wei; Su-Huai; Al-Jassim, M. Electronic structure of ZnO:GaN compounds: Asymmetric bandgap engineering. *Phys. Rev. B.* **2008**, *78*, 195204

[7] Higashi, M.; Domen, K.; Abe, R. Highly Stable Water Splitting on Oxynitride TaON Photoanode System under Visible Light Irradiation. *J. Am. Chem. Soc.* **2012**,*134*, 6968-6971.

[8] Reshak, A.H.; Ab initio study of TaON, an active photocatalyst under visible light irradiation. *Phys.Chem.Chem.Phys*., **2014**, 16, 10558-10565.

[9] Kim, Y.; Lee, E. Constant-wavelength neutron diffraction study of cubic perovskites. $BaTaO_2N$ and $BaNbO_2N$. *J. Ceram. Soc. Jap.* **2011**, *119*, 371-374

[10] Marchand, R.; Pors, F.; Laurent, Y.; Regreny, O.; Lostec, J.; Haussonne, J.M. Nitride oxide perovskites used as dielectric materials. *J. de Physique, Colloque* **1986**, *(C1)*, C1-901-C-905.

[11] Pors, F.; Marchand, R.; Laurent, Y.; Bacher, P.; Roult, G. Structural study of barium tantalum oxynitride ($BaTaO_2N$) and barium niobium oxynitride ($BaNbO_2N$) perovskites. *Mater. Res. Bul.l* **1988**, *23*, 1447-1450.

[12] Marchand, R.; Laurent, Y.; Guyader, J.; I'Haridon, P.; Verdier, P. Nitrides and oxynitrides: preparation, crystal chemistry and properties. *J. Eur. Ceram. Soc.* **1991**, *8(4)*, 197-213.

[13] Higashi, M.; Domen, K.; Abe, R. Fabrication of an Efficient $BaTaO_2N$ Photoanode Harvesting a Wide Range of Visible Light for Water Splitting. *J. Am. Chem. Soc.* **2013**, *135*, 10238−10241.

[14] Reaney, I. M.; Ubic, R. Dielectric and Structural Characteristics of Perovskites and Related Materials as a Function of Tolerance Factor. *Ferroelectrics* **1999**, *228*, 23-28.

[15] Kim, Y.; Woodward, P. M.; Baba-Kishi, K. Z.; Tai, C. W. Characterization of the Structural, Optical, and Dielectric Properties of Oxynitride Perovskites AMO2N (A = Ba, Sr, Ca; M = Ta, Nb) *Chem. Mater.* **2004**, *16*, 1267-1276.

[16] Kim, Y.; Weidong, S.; Woodward, P. M.; Sutter, E.; Park, S.; Vogt, T. Epitaxial Thin-Film Deposition and Dielectric Properties of the Perovskite Oxynitride $BaTaO_2N$. *Chem. Mater.* **2007**, *19*, 618-623.

[17] Segall, M. D.; Lindan, P.L.D.; Probert, M. J.; Pickard, C. J.; Hasnip, P. J. ; Clark, S. J.; Payne, M. C. J. First-Principles Simulation: Ideas, Illustrations and the CASTEP Code. *Phys. B: Condens. Matter* **2002**, *14*, 2717-2744.

[18] Perdew, J. P.; Burke, K.; Ernzerhof, M. Generalized Gradient Approximation Made Simple. *Phys Rev Lett.* **1996**, *77*, 3865-3868.

[19] Perdew, J. P., *Electronic Structure of Solids, P. Ziesche, H. Eschrig, Eds;* (Akademie Verlag: Berlin **1991**, pp. 11-20.

[20] Mulliken, R. S. Electronic Population Analysis on LCAO-MO Molecular Wave Functions. I. *J. Chem. Phys.* **1955**, *23*, 1833-1840.

[21] Palik, E. D., *Handbook of Optical Constants of Solids*; Academic Press: New York, 1985.

[22] Reshak, A.H; Roknabadi, M.R.; Mollaee, M.; Zaboli, M.; Bedhani M. Influence of Mechanical Alloying on Dielectric Features of Ferroelectric $BaTiO_3$ Microcrystals. *Int. J. Electrochem. Sci*. **2014**, 9, 720-727.

[23] Fang, C.M.; Orhan, E.; de Wijs, G.A.; Hintzen, H.T.; de Groot, R.A.; Marchand, R.; Saillard, J.Y.; de With, G. The Electronic Structure of Tantalum (Oxy) nitrides TaON and Ta_3N_5 *J. Mater. Chem.* **2001**, *11*, 1248-1252.

[24] Sanchez-Portal, D.; Artacho, E.; Soler, J. M. Projection of Plane-Wave Calculations into Atomic Orbitals. *Solid State Commun.* **1995**, *95*, 685-690.

[25] Wolff, H.; Dronskowski, R. First-Principles and Molecular-Dynamics Study of Structure and Bonding in Perovskite-Type Oxynitrides ABO_2N (A = Ca, Sr, Ba; B = Ta, Nb). *J Comput Chem.* **2008**, *29*, 2260-2267.

[26] Miller, A.; *Handbook of Optics: Fundamentals, Techniques, and Design, Volume 1*; McGraw-Hill, **1994**.

[27] Reshak, A.H.; Chen, X.; Auluck, S.; Kityk, I. V. *J. Chem. Phys.* **2008**, 129, 204111.

[28] Khan, S.A.; Reshak, A.H. First Principle Study of Electronic Structure, Chemical Bonding and Optical Properties of 5-azido-1H-tetrazole. *Int. J. Electrochem. Sci.* **2013**, *8*, 9459-9473.

[29] Fox, M., *Optical Properties of Solids*; Oxford University Press; **2001**.

[30] Taflove, A., *Computational electrodynamics: Finite Difference Time Domain Method*; Boston, MA: Artech House, **1995**.

[31] Aoyagi, P. H.; Lee, J.F.; Mittra, R. A hybrid Yee algorithm/scalar wave equation approach. *IEEE Trans. Microw. Theory Tech.* **1993**, 41, 1593-1600.

Figure Captions:

Figure 1: (a) The crystal structure and (b) the Band structure of $BaTaO_2N$, with the two nitrogen atoms in the N-Ta-N bond making straight angel (180°), and (c) Total and partial Density of states of $BaTaO_2N$.

Figure 2: Projected contour maps for the electronic wave functions for $BaTaO_2N$. (a, c and e) represent the bonding states, and (b, d and e) represent the anti-bonding states.

Figure 3: (a) The real and (b) imaginary parts of the diagonal components of the dielectric constants for $BaTaO_2N$.

Figure 4: The calculated (a) refractive index $n(\omega)$, (b) extinction coefficient $k(\omega)$, (c) absorption coefficient $\alpha(\omega)$, (d) reflectivity $R(\omega)$ and (e) energy-loss spectrum $L(\omega)$ for $BaTaO_2N$.

Figure 5: (a) Schematic diagram for the model used in the FDTD simulations, (b) The simulated transmittance, reflectance and absorbance for $BaTaO_2N$ powder, and (c) snapshots at certain time instances for the Electromagnetic wave propagation inside the material.

Figures

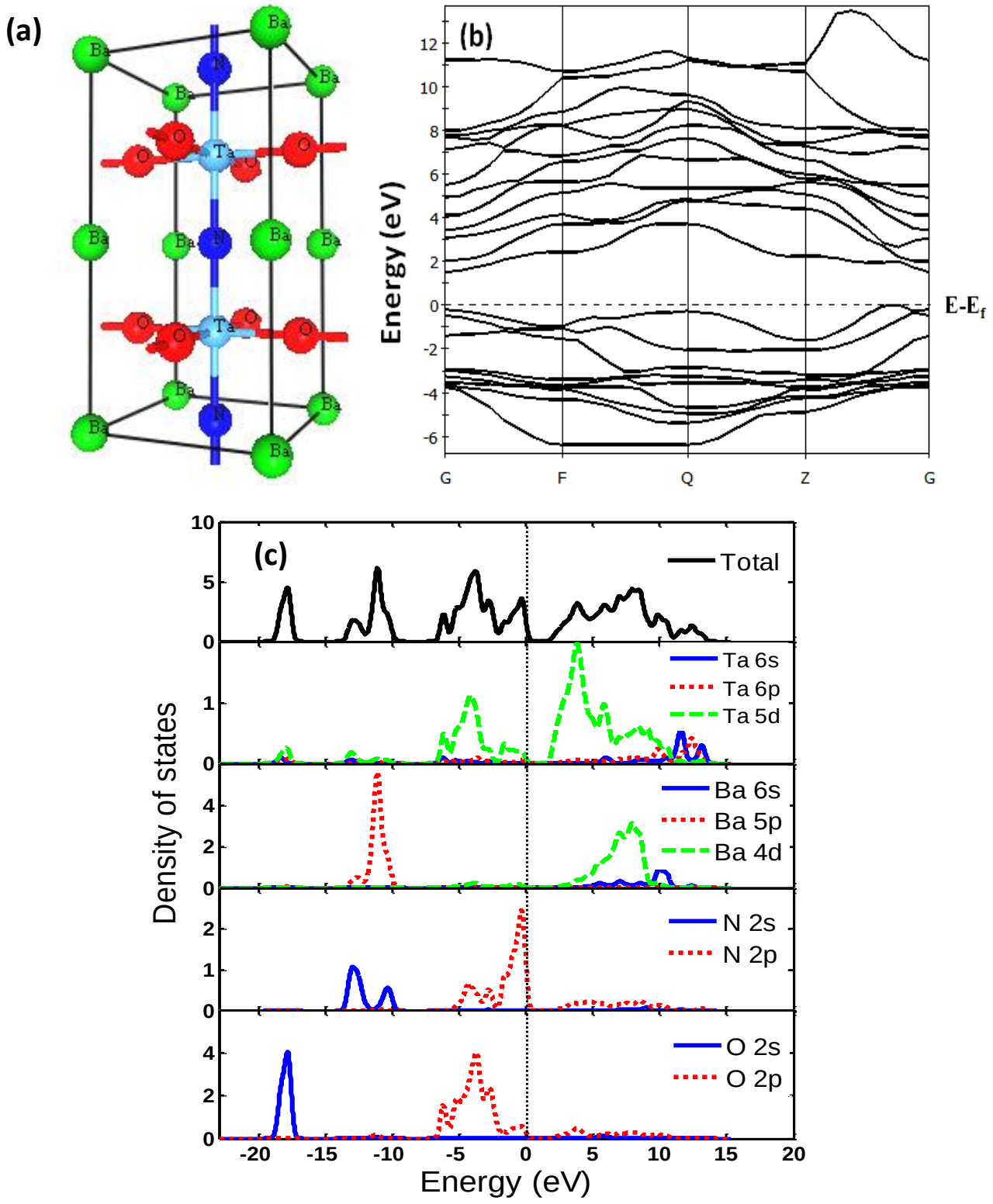

Figure 1

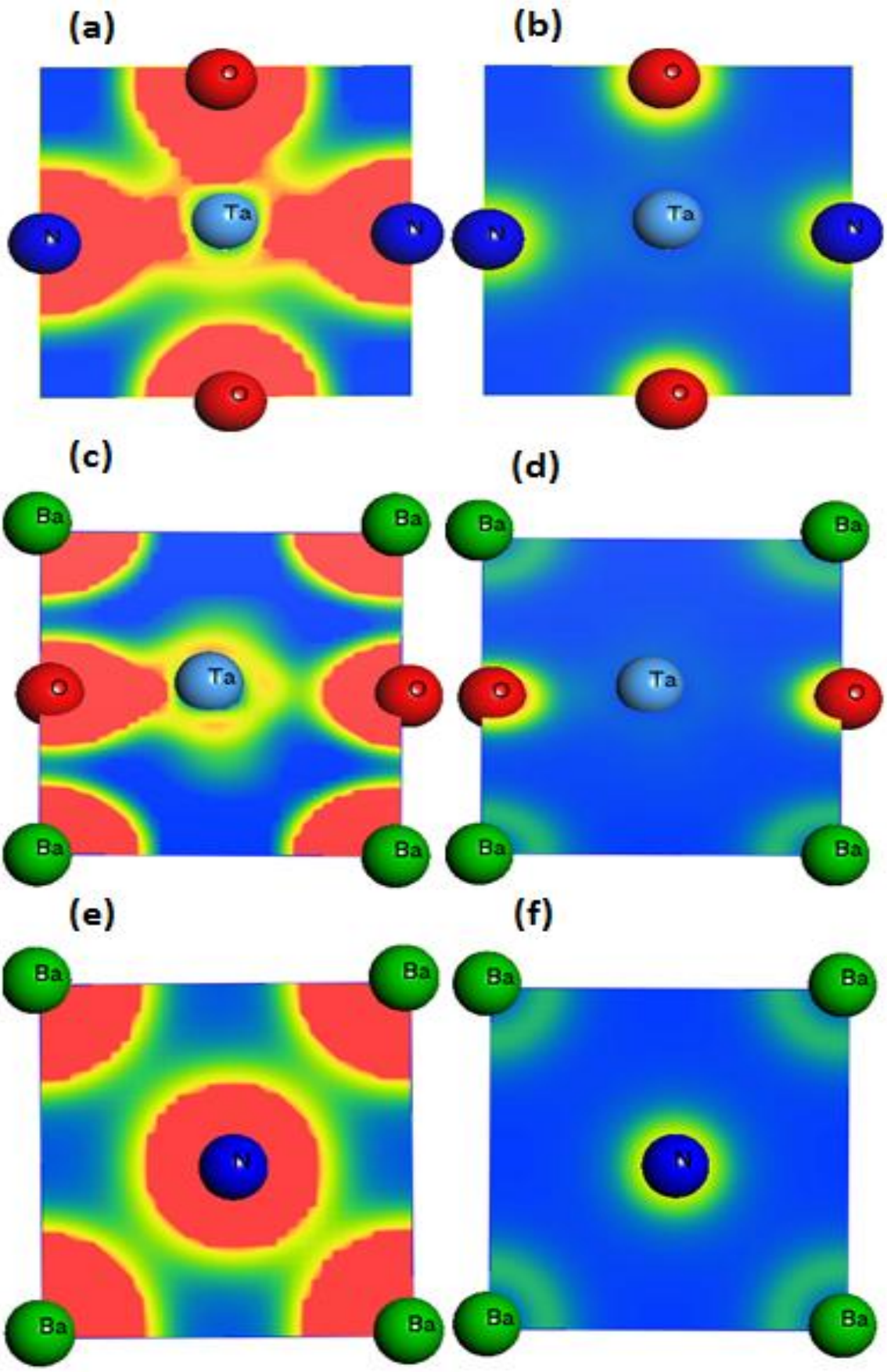

Figure 2

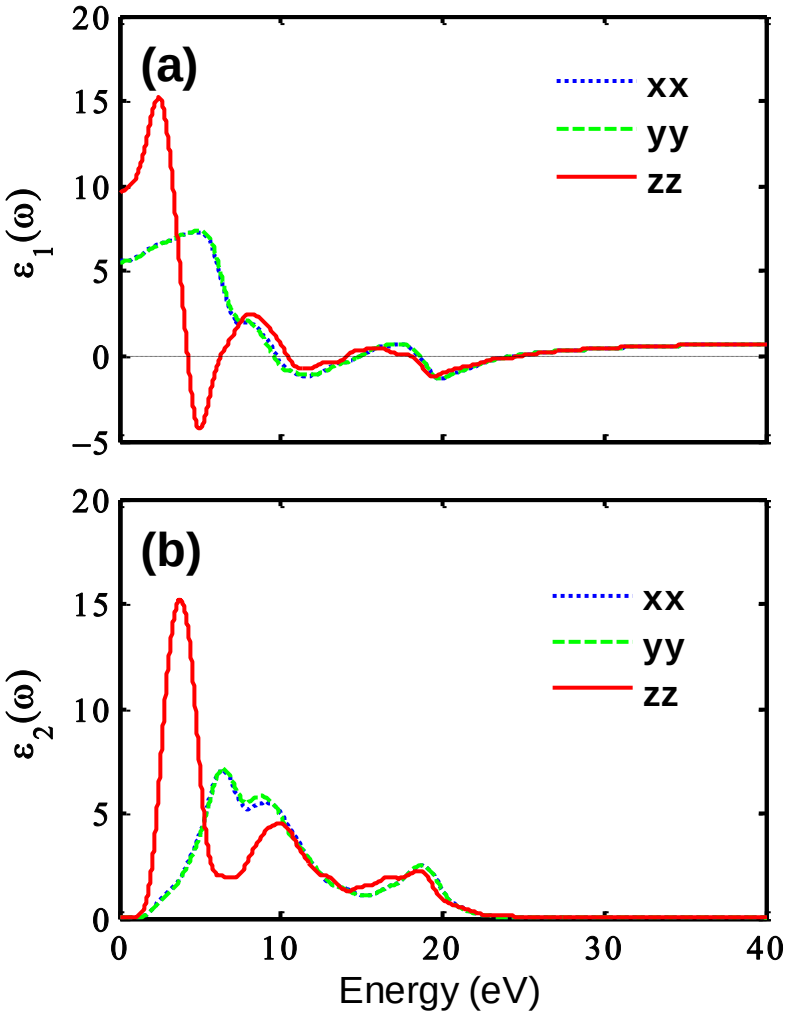

Figure 3

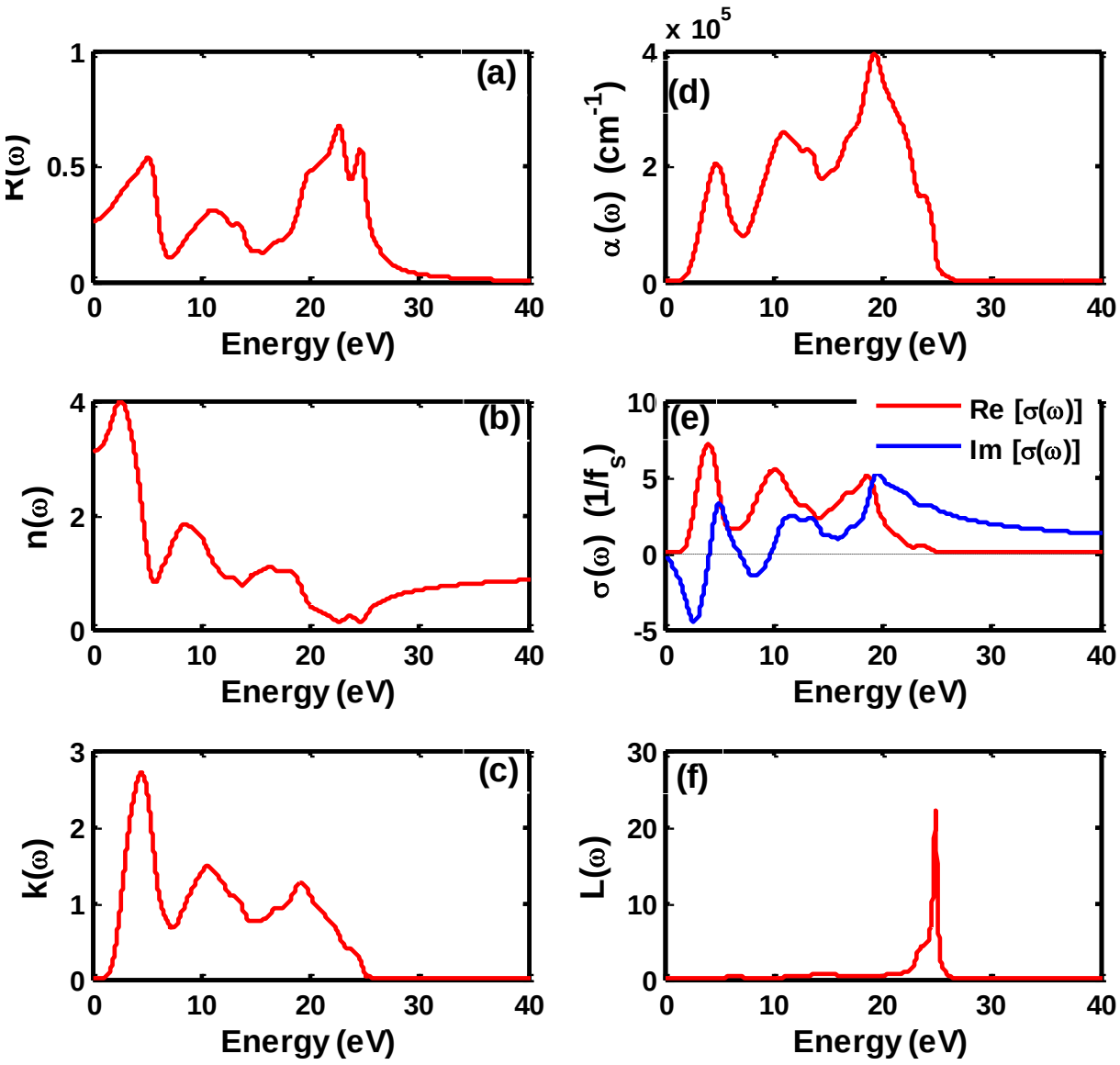

Figure 4

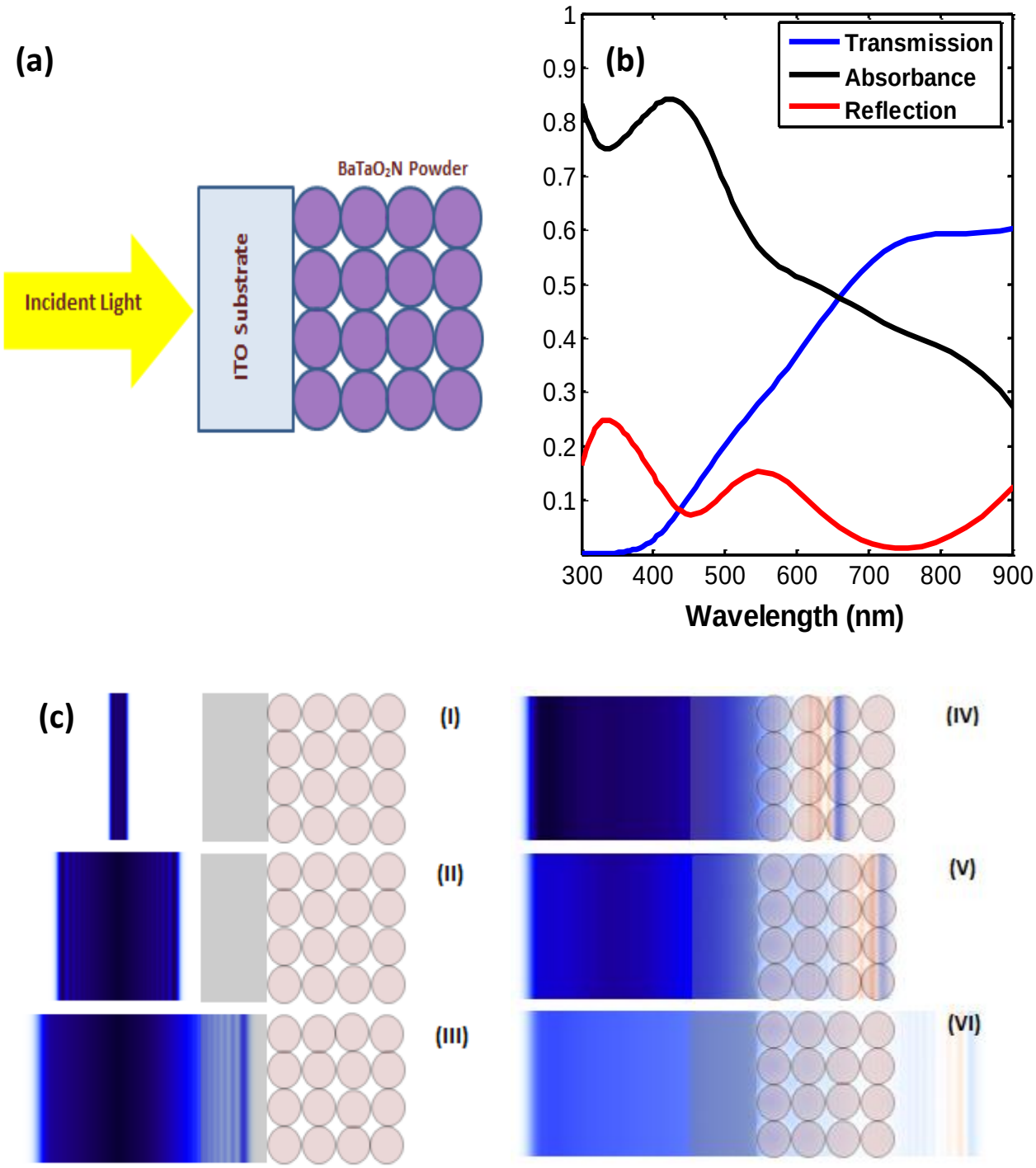

Figure 5

Tables

Table I: Lattice parameters and atomic positions for $BaTaO_2N$

			present						experiment				
Lattice parameters	a (Å)	b(Å)	C(Å)	α	β	γ	a (Å)	b(Å)	C(Å)	α	β	γ
	4.144	4.178	3.958	89.99°	89.99°	90.55°	4.113	4.113	4.113	90°	90°	90°
Atom positions		x		y		z		x		y		z
	Ba	-0.02		0.02		0.0	Ba	0.0		0.0		0.0
	Ta	0.46		0.534		0.5	Ta	0.5		0.5		0.5
	O1	0.02		0.491		0.499	O1	0.0		0.5		0.5
	O2	0.51		-0.02		0.499	O2	0.5		0.0		0.5
	N	0.52		0.48		0.0	N	0.5		0.5		0.0

Table II: Mulliken atomic populations and bond length for $BaTaO_2N$

Mulliken atomic populations and bond length					
Species	s	p	d	Total	charge
N	1.72	4.16	0	5.85	-0.88
O1	1.85	4.92	0	6.77	-0.77
O2	1.85	4.92	0	6.76	-0.76
Ba	2.12	5.98	0.76	8.86	1.14
Ta	0.29	0.31	3.14	3.74	1.26
Bond		Population		Length (Å)	
O1-Ta		0.48		2.34701	
O2-Ta		0.47		2.32061	
N-Ta		0.72		2.00014	
O1-Ba		0.08		2.79707	
O2-Ba		0.09		2.79548	
N-Ba		0.18		2.73465	
N-O		-0.14		2.85941	

Table of Contents Image